Design of a low Young's modulus Ti-Zr-Nb-Sn biocompatible alloy by in situ laser powder bed fusion additive manufacturing process

Hugo Schaal, Philippe Castany, Pascal Laheurte, Thierry Gloriant

Design of a low Young's modulus Ti-Zr-Nb-Sn biocompatible alloy by *in situ* laser powder bed fusion additive manufacturing process

Hugo SCHAAL[1,2], Philippe CASTANY[1], Pascal LAHEURTE[3], Thierry GLORIANT[1*]

[1] Université de Rennes, INSA Rennes, CNRS, ISCR UMR 6226, 35000 Rennes, France

[2] SLS France, 32 Boulevard de la Haie des Cognets, 35136 Saint-Jacques-de-la-Lande, France

[3] Université de Lorraine, CNRS, LEM3 UMR CNRS 7239, 57045 Metz, France

***Corresponding author:** thierry.gloriant@insa-rennes.fr

Abstract: A new metastable β Ti-22Zr-11Nb-2Sn (at%) biomedical titanium alloy was elaborated from elemental powders by *in situ* laser powder bed fusion technique (L-PBF). Iterative design of experiments was used to identify optimized manufacturing parameters to obtain dense and homogeneous parts (>99.3%) with low unmolten niobium fraction (<0.05%). The microstructural and mechanical properties of this alloy were investigated in its as-fabricated state and after two heat-treatments at 400°C and 700°C, respectively. The alloy, showing a β-type microstructure, possesses a very low Young's modulus (~50 GPa) combined with a high tensile strength reaching about 1100 MPa after heat-treatment. These properties are very suitable for medical devices in osseous site such as hip prostheses or dental implants and the results were compared to the Ti-6Al-4V ELI (wt%) medical grade fabricated from pre-alloyed powders. Thus, the present work demonstrates the significant potential of the *in situ* L-PBF technique to elaborate highly biocompatible titanium alloys with tailored chemical compositions.

Keywords: additive manufacturing, *in situ* elaboration, titanium alloys, low Young's modulus, high strength.

1. Introduction

Titanium alloys are widely used for biomedical applications, from dental implants to joint and hip replacements. Ti-6Al-4V (wt%) and its extra low interstitial (ELI) medical grade are the most common titanium alloys used for these purposes, due to their excellent mechanical properties, their good strength to weight ratio, and their resistance to bio-corrosion. However, there is controversy over the alloying elements Al and V in terms of biocompatibility [1-5]. Indeed, cytotoxicity of Al and V elements can be problematic due to their release in the biological tissues [6, 7]. On the other hand, the difference between the elastic modulus of this kind of alloys (about 110 GPa) and the modulus of the cortical bone (~30 GPa [8, 9]) has been pointed out as a major issue for long-term implantation, known as "stress-shielding" [10, 11]. This phenomenon causes a bone resorption around the titanium made implant and can lead to loss of the implant.

From these considerations, the development of aluminium and vanadium free titanium alloys with low elastic modulus for biomedical applications has been an area of interest for the last decades [12-17]. β and metastable-β titanium alloys have been identified as appropriate candidates for these applications. Indeed, the stabilisation of the β phase in this kind of alloys can lead to lower Young's modulus than Ti-6Al-4V [9], thus avoiding the "stress-shielding" effect. Furthermore, these alloys can be obtained from highly biocompatible elements such as zirconium, tin, niobium, and tantalum, the latter two being in addition β-stabilizers [14, 18]. They can also exhibit a stress-induced martensitic transformation from the body-centered cubic β phase to the orthorhombic α'' phase, leading to unconventional mechanical behaviour such as superelastic and shape memory effects [19, 20].

The emergence of additive manufacturing processes, and especially the laser powder bed fusion technique (L-PBF), has attracted significant interest in the biomedical field, due to the capability to manufacture patient-specific devices. Most of the research and development around L-PBF processed titanium alloys is focused on the characterization of microstructures and mechanical properties of the Ti-6Al-4V alloy obtained from pre-alloyed powders [21-23]. Due to the lack of diversity of pre-alloyed metallic powders, the L-PBF elaboration of β and metastable-β titanium alloys is still marginally reported and investigated. *In situ* elaboration, promoting the use of a blend of elemental powders of a given composition, has been identified as a more flexible technique to study specific alloys [24-27]. However, refractory β-stabilizers elements with high melting point such as niobium, tantalum and molybdenum tend to remain unmelted or partially melted in the alloy metallic matrix, causing local chemical heterogeneities [28, 29]. However, the optimisation of the manufacturing parameters through design of experiments seems effective to reduce both porosity and alloying elements inclusions. Biocompatible binary β-titanium alloys such as Ti-Ta [29, 30] and Ti-Nb [28, 29, 31, 32] have been studied using the *in situ* L-PBF technique. However, the quantity of alloying elements used in these studies to stabilize the β phase either led to a high unmelted fraction of alloying elements or required an extremely high energy input to homogenize the alloy under the laser beam.

In this study, the β-titanium Ti-22Zr-11Nb-2Sn (at%) alloy composition was manufactured using the *in situ* L-PBF elaboration technique. This composition was selected on the basis of recent work that we have carried out on quaternary alloys elaborated by conventional melting methods [18], which seem suitable for *in situ* elaboration by L-PBF. The use of a relatively low niobium fraction (11 at%) aims to reduce the quantity of niobium inserted in the powder mix, and by extension the unmelted fraction of niobium elements in the metallic matrix. To ensure the stabilization of the β phase, zirconium is added up to 22 at%. Even though the influence of zirconium on the stabilisation of either α or β phase of titanium is considered as neutral, it has been shown that zirconium acts as a β-stabilizing element when combined with β-stabilizing elements such as molybdenum or niobium [33, 34].

This study aims to propose an optimization process to identify the optimal elaboration window for this new β-titanium alloy, and to characterize the microstructural and mechanical properties of the obtained alloy. The influence of heat-treatments on the microstructural characteristics and the mechanical properties is also investigated. Since the Ti-6Al-4V ELI alloy is the most widely used titanium alloy for medical devices, reference specimens were built from pre-alloyed Ti-6Al-4V ELI powders for comparison.

2. Materials and methods

2.1. Description of the powders used

The properties of elemental powders used to carry out the *in situ* elaboration of the Ti-22Zr-11Nb-2Sn are detailed in Table.1. Gas atomized titanium and zirconium powders were obtained from ECKART TLS. Gas atomized niobium powders were obtained from H.C. Starck. Mechanically ground tin powders were obtained from Sigma Aaldrich. The powders were blended for 2 hours at 34 rpm using a Turbula T2F device. Fig.1a shows a back-scattered scanning electron microscopy (SEM) image of the mix after blending. It should be noted that the niobium powder is the finest of all (Table.1). The use of a fine niobium powder for *in situ* elaboration is required according to the literature to reduce as much as possible the unmelted particles fraction [25].

Table 1
Ti-22Zr-11Nb-2Sn (at%) elemental powders properties.

Element	Size distribution (µm)	D50(µm)	Purity	Morphology	Melting T (°C)
Ti	15-45	35.7	>99.7	Spherical	1668
Zr	10-45	32	>99.7	Spherical	1855
Nb	10-45	29.9	>99.9	Spherical	2469
Sn	< 45	-	>99.9	Irregular	232

ASTM F3001 standard compliant Ti-6Al-4V ELI pre-alloyed powders from AP&C powders were used to build reference specimens. The average powder size is between 15-45 µm. Fig. 1b shows a back-scattered SEM micrograph of the Ti-6Al-4V ELI powder.

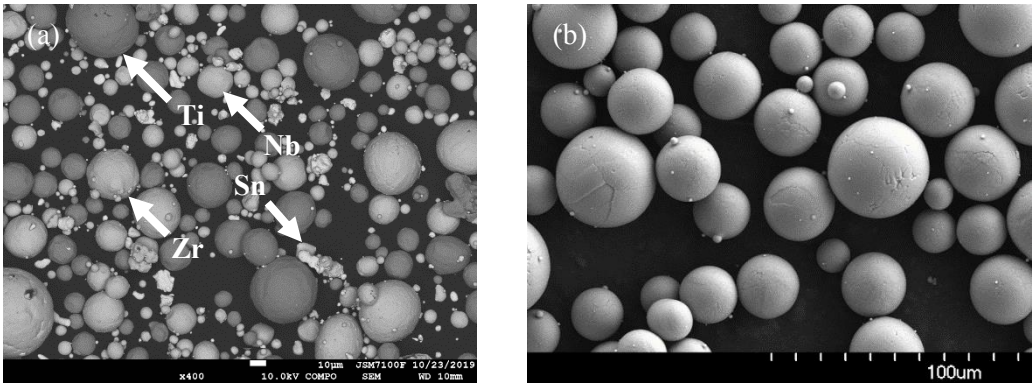

Fig.1: *Ti-22Zr-11Nb-2Sn powder mix (a) and Ti-6Al-4V ELI pre-alloyed powders (b) used during this study.*

2.2. Additive manufacturing by L-PBF

A SLM 125 HL (SLM Solutions Group AG, Germany) equipped with a 400W laser was used to carry out the elaboration of the different titanium alloys. The manufacturing chamber was filled with an Ar atmosphere during elaboration to maintain the oxygen below 500 ppm. Different types of specimens were built to characterize the microstructural and mechanical properties of the different alloys: 10x10x10 mm^3 cubes were used to characterize the microstructural properties of the specimens. Flat tensile specimens with a gauge section of 3x1 mm^2 and a gauge length of 15 mm were extracted by electrical discharge machining from 50x5x2 mm^3 rectangles and used for mechanical characterization. Cylindrical samples of 3mm diameter and 15 mm long were also built to characterize the porosity and the unmelted alloying element fraction of the specimens using X-ray Tomography. A 67° hatch scanning strategy was used for both Ti-6Al-4V ELI and Ti-22Zr-11Nb-2Sn alloys during elaboration. Concerning the fabrication of the Ti-6Al-4V ELI parts, a laser power of 175W, a laser speed of 1000 $mm.s^{-1}$, a hatch space of 100 µm, and a layer thickness of 20µm were used. These manufacturing parameters correspond to those recommended by the supplier of pre-alloyed Ti-6Al-4V ELI powders. Optimized elaboration parameters for the elaboration of the new Ti-22Zr-11Nb-2Sn alloy were investigated using design of experiments. The results are presented and discussed in section 3.1.

2.3. Microstructural and mechanical characterization methods

Microstructure and texture of both alloys were characterized by X-ray diffraction (XRD), electron back-scattered diffraction (EBSD) and transmission electron microscopy (TEM). EBSD analyses were carried out on a JEOL JSM 7100F scanning electron microscope with a step of 0.1 µm and an accelerating voltage of 20 kV. Specimens for EBSD analysis were prepared by mechanical polishing using SiC papers with decreasing grid size, followed by colloidal silica suspension polishing mixed with H_2O_2 to get a “mirror finished” state. Texture

was investigated through $\{200\}_\beta$, $\{110\}_\beta$ and $\{112\}_\beta$ poles figures acquisition on a Rigaku SmartLab X-ray diffractometer using Cu-$K_{\alpha 1}$ radiation at 40 kV and 50 mA. TEM observations were carried out on a JEOL JEM 2100 LaB_6 machine. TEM specimens were prepared by a three steps ion milling process with 4 keV, 2 keV and 0.5 keV argon ions using a Gatan PIPS II machine.

Porosity and unmelted alloying elements of the Ti-22Zr-11Nb-2Sn alloy were investigated through X-ray µ-tomography. An EasyTom (Rx Solutions) device was used to carry out the measurements.

Mechanical characterization of both titanium alloys was carried out through tensile tests on a Instron tensile device with a 5 kN load cell. Those tests were performed with a strain rate of 10^{-4} s^{-1}, and deformation was measured with an extensometer. The tensile direction for both titanium alloys was chosen orthogonal to the building direction. 10 different specimens were tested for each condition and the mechanical properties are presented via mean values and their standard deviations. Tensile curves shown in this study are those which best correspond to the mean value of the mechanical behaviour of the studied specimens.

3. Results and discussion

3.1. Optimization of the L-PBF process for the in situ elaboration of the Ti-22Zr-11Nb-2Sn alloy

The optimization of building parameters of the L-PBF process has been a focus of interest since the early development of additive manufacturing technologies. Indeed, building parameters have a great influence on the structural and microstructural characteristics of the metallic alloys elaborated [35-39]. Considering the important number of elaboration parameters, design of experiments (DOE) has proven to be useful [40] to analyse the influence of the variation of building parameters on a restricted number of outputs, such as porosity and unmelted alloying particles. In our case, iterative design of experiments was used to identify the optimized building parameters to obtain dense and homogeneous parts. This optimization method was based on the Box-Behnken response surface methodology. The iterative method used for the optimization of the building parameters is schematized in the flow chart in Fig.2.

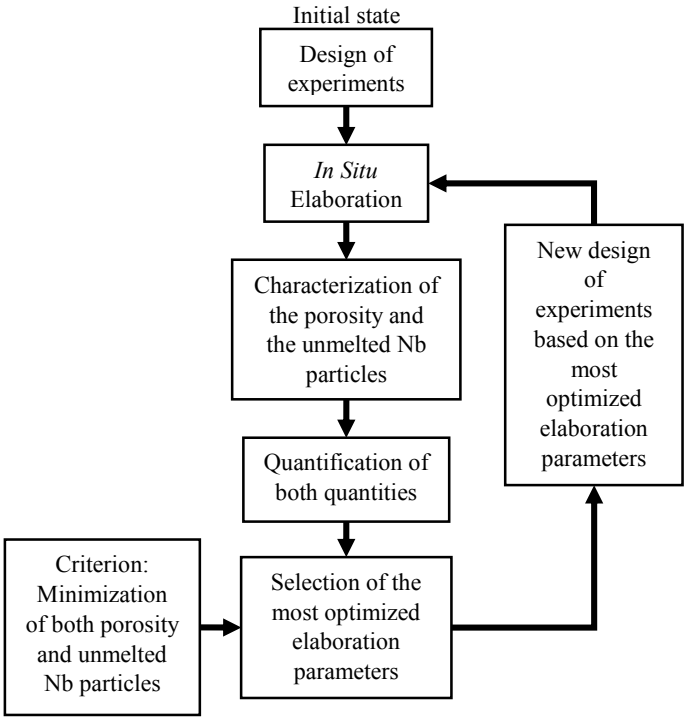

Fig.2: *Flow chart used for the iterative method of optimization of the manufacturing parameters.*

The influence of the variation of laser power, scanning speed of the laser, hatch-distance and ~~the~~ layer thickness on the porosity fraction and the unmelted niobium fraction is investigated in the present study. The selection criterion of the appropriate optimized parameters is based on the minimization of both porosity and unmelted Nb particles. Through the first iterations of the design of experiment, two sets of parameters seem to ensure satisfying results for both unmelted niobium fraction and porosity. The last step of optimization is focusing on the influence of the scanning speed of the laser on the defined outputs, based on the previous sets of optimized parameters. Table.2 displays the different building parameters tested during the last step of the design of experiments.

Table 2
Building parameters from the last iteration of the DOE.

Specimen	*P* (W)	*v* (mm.s^{-1})	*h* (mm)	*e* (µm)	Porosity (%)	Unmolten Nb (%)
1	200	555	0.06	20	3.39	0.03
2	200	355			1.76	0.08
3	200	305			0.7	0.04
4	250	695			1.7	0.02
5	250	480			1.15	0.05
6	250	380			0.3	0.05

As those different building parameters derive from previously optimized building parameters, they allow to keep the unmelted fraction of niobium below 0.1% of the volume of the

specimen. This result highlights the efficiency of the combination of adapted granulometry of niobium powders (Table.1) and optimization of building parameters using design of experiments. Tomographic reconstruction of cylindrical samples of the first iteration of design of experiments and the final optimized parameters are presented in Fig.3.

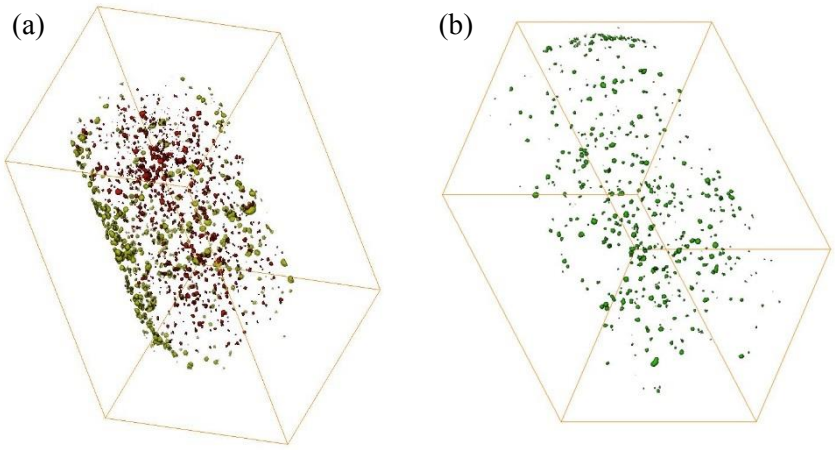

Fig.3: *Tomographic reconstruction of the Ti-22Zr-11Nb-2Sn cylindrical samples of the first step of design of experiments (a), and final step of design of experiments (b).*

Both porosity and unmelted niobium particles decrease along the iterative DOE, as the window processability is more and more precise. Both 3 and 6 specimens exhibit lowest porosities and unmelted niobium particles, but the elaboration conditions of the 6th specimen also led to a deformation of the sample, due to the high energy input. Building conditions n°3 were then used to carry out to elaborate all specimens.

3.2. Microstructural characterisation of the as-fabricated specimens

Microstructures of as-fabricated (AF state) Ti-6Al-4V ELI and Ti-22Zr-11Nb-2Sn alloys are shown in Fig.4. XRD pattern of the AF-Ti-22Zr-11Nb-2Sn (Fig.4c) exhibits typical body-centered cubic diffraction peaks, meaning that the alloy is mainly composed of β phase (a_β = 0.337 nm). The combination of β-stabilizing alloying elements content and cooling conditions of the L-PBF process can promote a fully-β microstructure without heat-treatment or quenching. Macrostructure of this new β-titanium alloy displays regular semi-elliptical shapes, which correspond to the longitudinal sections of consecutive laser tracks (Fig.4a). The range of shapes that can be observed is due to the 67° scanning strategy, changing the laser trajectories layer after layer. This kind of morphology has already been reported for materials elaborated via L-PBF process [24, 41] and seems to be dependant of elaboration parameters that shape and drive the melt pool [42]. No grains are visible despite the chemical etching of the alloy.

XRD pattern of the AF-Ti-6Al-4V sample (Fig.4d) is fully indexed as α' hexagonal phase ($a_{\alpha'}$ = 0.292 nm; $c_{\alpha'}$ = 0.467 nm), which is a martensitic phase that is commonly observed in titanium alloys after rapid cooling. Although the α' phase develops in the same hexagonal

crystallographic system than the α phase, its chemical composition is identical to the initial β phase. The microstructure of the alloy (Fig.4b) is composed of columnar grains along the building direction. Those grains have an average width of 175 µm. This columnar morphology is caused by the elaboration conditions of the L-PBF process, as the layer-by-layer elaboration and the partial remelting of previous layers promote an epitaxial growth along the building direction. A fine needles-like microstructure is also visible within the columnar grains, with a needle width of about 1 µm. α' martensitic phase is known to form into a fine needle-like structure in titanium alloys, the width of the needles being controlled by the cooling rate of the alloy. The microstructure of Fig.4b is consistent with the indexation of the corresponding XRD pattern (Fig.4d), because the cooling rates of the laser powder bed fusion process are known to be fast (~10^5 K/s [43]) promoting then the formation of refined martensitic phases.

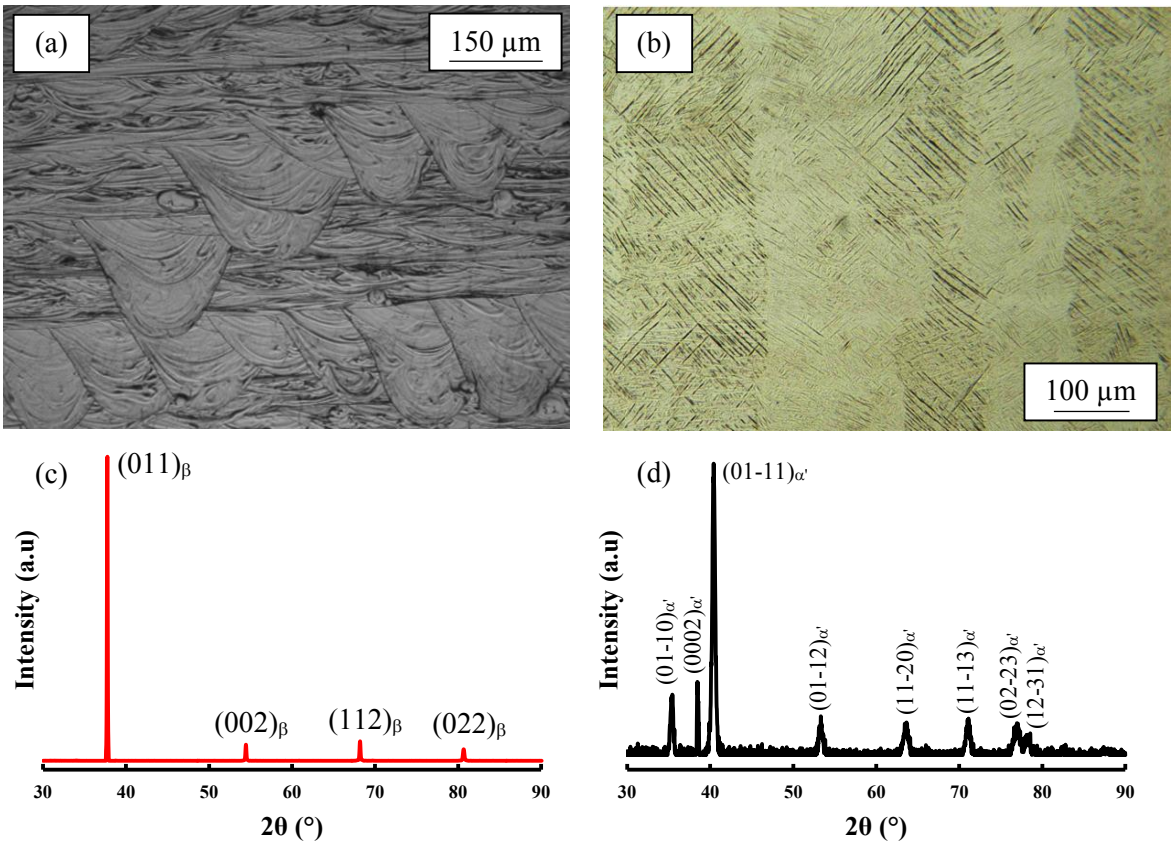

Fig.4: *Optical microscopy of the macrostructure of the AF-Ti-22Zr-11Nb-2Sn (a) and the microstructure of the AF-Ti-6Al-4V (b), along the XRD patterns of the AF-Ti-22Zr-11Nb-2Sn (c) and the AF-Ti-6Al-4V (d).*

Microstructure of both alloys was more precisely investigated through EBSD analysis (Fig.5). Inverse Pole Figure (IPF-EBSD) map of the AF-Ti-22Zr-11Nb-2Sn in Fig.5a displays a columnar microstructure along the building direction, just as the AF-Ti-6Al-4V microstructure (Fig.4b). Those elongated grains are about 140 µm long, for a width of about 45 µm. This analysis corroborates the XRD pattern indexation of Fig.4c, as every grain of the AF-Ti-22Zr-11Nb-2Sn microstructure is indexed as the cubic β phase. Texture of the AF-Ti-

22Zr-11Nb-2Sn is also investigated. The inverse pole figures shown (Fig.5a) imply a strong $<100>_{\beta}$ texture along the building direction (BD). It is worth noting that the texture observed in the tensile direction (TD) and the normal direction (ND), which are both orthogonal to BD, are similar. Those inverse pole figures show a concentration of $\{405\}_{\beta}$ poles in TD and ND directions, which are close to $\{110\}_{\beta}$. The texture in BD is a consequence of the epitaxial growth promoted by the layer-by-layer building and has already been reported for bcc materials in the literature [44-46].

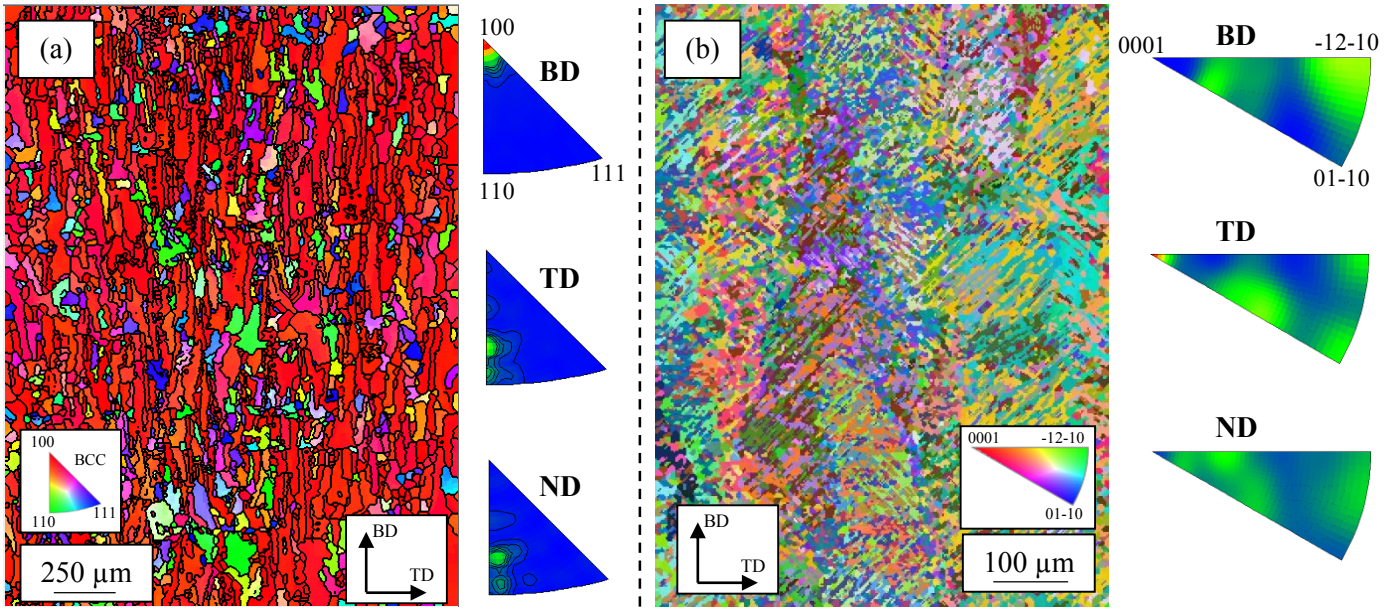

Fig.5: *IPF-EBSD maps along the building direction of the AF-Ti-22Zr-11Nb-2Sn (a) and the AF-Ti-6Al-4V (b).*

The IPF-EBSD map of the AF-Ti-6Al-4V (Fig.5b) corroborates the XRD analysis of Fig.4d, as it is fully indexed as α/α' phase. As specified above, both α' and α phases possess the same crystallographic system and cannot be distinctly identified via EBSD analysis. Elongated grains are however visible, as the martensitic α' needles of similar orientations formed from the same β grain, delimiting the initial elongated parent β-grains.

Texture of the AF-Ti-6Al-4V is also investigated via EBSD and inverse pole figures (Fig.5b). Inverse pole figures of BD exhibit two high pole density, $\{-12-10\}_{\alpha'}$ and $\{01-12\}_{\alpha'}$. Textures in TD and ND directions are not equivalent and exhibit very different preferential directions. TD shows a high $(0001)_{\alpha'}$ pole density while the texture in ND does not exhibit preferential direction. If we refer at the standard orientation relationship (OR) between the α' martensitic phase and the parent β phase from which it formed, i.e. $(0001)_{\alpha'}$ // $(110)_{\beta}$ and $[2-1-10]_{\alpha'}$ // $[1-11]_{\beta}$, texture of the AF-Ti-6Al-4V along BD is consistent with the texture observed along BD of AF-Ti-22Zr-11Nb-2Sn β-phase. As a matter of fact, following the standard OR between α' and β phases, $\{100\}_{\beta}$ poles are supposed to match one $\{11-20\}_{\alpha'}$ pole, and two $\{01-12\}_{\alpha'}$ poles. As these poles match the ones observed in the inverse pole figure of BD for the AF-Ti-6Al-4V (Fig.5b), it can be assumed that the initial parent β–grains displayed a $<100>_{\beta}$

preferential direction along BD. Texture along TD is also consistent with the standard OR, as β phase in AF-Ti-22Zr-11Nb-2Sn shows high poles density near $\{110\}_\beta$ in TD, which is supposed to match $(0001)_{\alpha'}$ in the α phase. However, texture along the ND direction of the AF-Ti-6Al-4V does not exhibit $(0001)_{\alpha'}$ preferential direction and therefore does not match the texture along the ND direction of the AF-Ti-22Zr-11Nb-2Sn alloy.

3.3. Microstructural characterization of the AF-Ti-22Zr-11Nb-2Sn after heat-treatments

Characteristic phase transformation temperatures of the AF-Ti-22Zr-11Nb-2Sn were identified through resistivity thermal analysis. This method relies on the measurement of the electrical resistivity upon a range of temperature. As electrical resistivity is particularly sensitive to microstructural modifications, this method is suitable to detect characteristic temperatures of metallic alloys such as the β transus temperature of titanium alloys. Fig.6 displays the variation of electrical resistivity (ρ_0 correspond to the resistivity at room temperature) of the AF-Ti-22Zr-11Nb-2Sn alloy as a function of temperature. The β transus temperature of this alloy (T_β) is about 500°C, which is consistent with the fact that this alloy is a metastable β-type alloy in its AF state. Consequently, variations of the electrical resistivity between 300°C and 500°C implies a modification of the microstructure, such as the nucleation of α or ω_{iso} phases as reported in the literature [47, 48].

The influence of heat-treatments on the microstructural and mechanical properties of the AF-Ti-22Zr-11Nb-2Sn are investigated through two different heat-treatment temperatures: a 400°C heat-treatment for 30 minutes followed by water-quenching (400WQ state), and a 700°C standard solution treatment for 30 minutes followed by water-quenching (700WQ state). Heat-treatments were carried out under high-vacuum atmosphere (10^{-8} mbar) to prevent the oxidation of the samples.

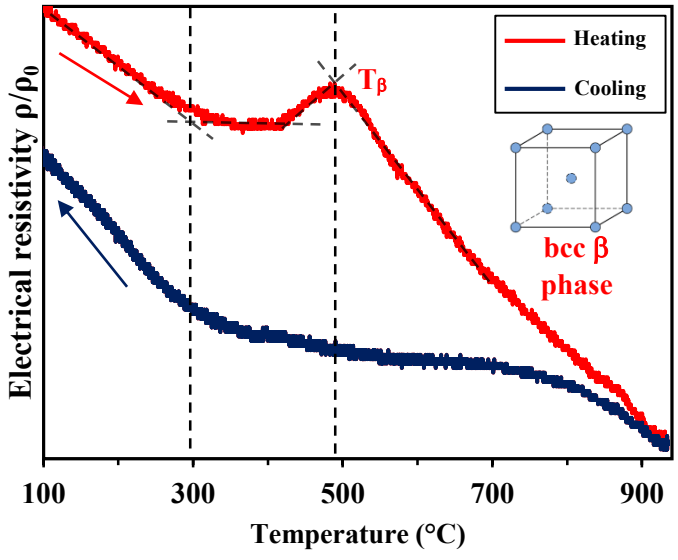

Fig.6: *Resistivity analysis curve for the AF-Ti-22Zr-11Nb-2Sn alloy.*

Fig.7 displays XRD patterns of the three different conditions (AF, 400WQ and 700WQ states). Since the diffraction patterns of the AF and 700WQ states are identical (Fig.7a&b), this implies that the 700WQ specimen is fully composed of β phase (a_β = 0.337 nm). As the heat-treatment temperature is above the β transus and is followed by water quenching, a fully-β microstructure is expected. However, the shift of the relative intensity of the $(002)_\beta$ peak observed between the AF and 700WQ states may imply a modification of the crystallographic texture of the specimen through heat-treatment.

The XRD pattern of the 400WQ specimen (Fig.7c) exhibits the characteristic peaks of the β phase (a_β = 0.338 nm) which correspond to the same peaks of the AF and 700WQ states. However, other diffraction peaks are also visible, and indexed as the hexagonal α phase of titanium (a_α = 0.303 nm; c_α = 0.462 nm). As the relative intensity of β phase peaks are significantly higher than those of α phase peaks, it can be assumed that the 400WQ specimen is composed of a majority of β phase. This result is consistent with the resistivity curve (Fig. 6) and therefore a nucleation of α phase during the heating of the AF-Ti-22Zr-11Nb-2Sn alloy occurs between 300°C and 500°C, leading to a dual-phase β+α microstructure.

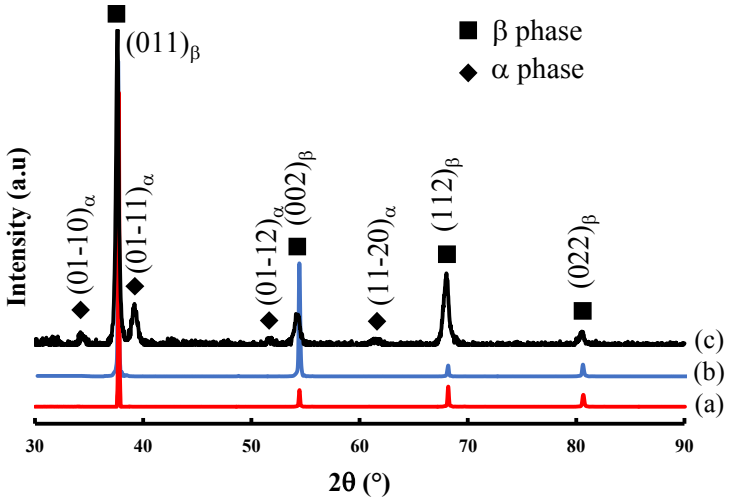

Fig.7: *XRD patterns of the AF-Ti-22Zr-11Nb-2Sn (a) the 700WQ state (b) and 400WQ state (c).*

Details about microstructures of both heat-treated specimens are given through EBSD and texture analyses (Fig.8).

IPF-EBSD map of the 700WQ specimen exhibits regular, quasi-equiaxed shaped grains, with a mean diameter of 24 µm (Fig.8a). Texture of the 700WQ state (Fig.8c and Fig.8e) is very different from the texture of the as-fabricated state in this Ti-22Zr-11Nb-2Sn alloy (Fig.5a). Indeed, the tensile direction (TD) exhibits a preferential $<100>_\beta$ direction, with an intensity factor of 4.12. It should be noted that the texture along BD still exhibits a significant number of grains nearly oriented $<100>_\beta$ (intensity factor 1.87). The changes in both granular

morphology and texture of the specimen imply that the alloy experienced recrystallization during heat-treatment. It is well-known that as-fabricated additive manufacturing parts exhibit high level of residual stresses [49, 50], which can constitute a driving force for the recrystallization of metallic alloys. With a heat-treatment temperature of 700°C, which is above the transus β temperature (T_β~500°C), a recrystallized microstructure is obtained in those conditions.

IPF-EBSD map of the 400WQ sample (Fig.8b) exhibits elongated grains along the building direction, with an average length of 120µm, for 40µm average width. Inverse pole figures of this specimen exhibit a preferential $<100>_\beta$ direction along BD, and no preferential directions along both TD and ND (Fig.8d and Fig.8f). With a heat-treatment at 400°C, the transus β temperature is not reached and the sample has not recrystallized. The texture can therefore be considered equivalent to the as-fabricated texture. The intensity factor of the $<100>_\beta$ preferential direction is around 14 for the 400WQ state of the Ti-22Zr-11Nb-2Sn alloy, which highlights the modification of the texture observed in the recrystallized state of the same alloy (Fig.8c). Despite coarser grains, the 400WQ state microstructure is identical to the AF-Ti-22Zr-11Nb-2Sn microstructure. However, the grains of the 400WQ specimen are fully indexed as β phase by EBSD, which is not consistent with the XRD analysis of this specimen for which a second phase, identified as the α phase, was detected (Fig.7c).

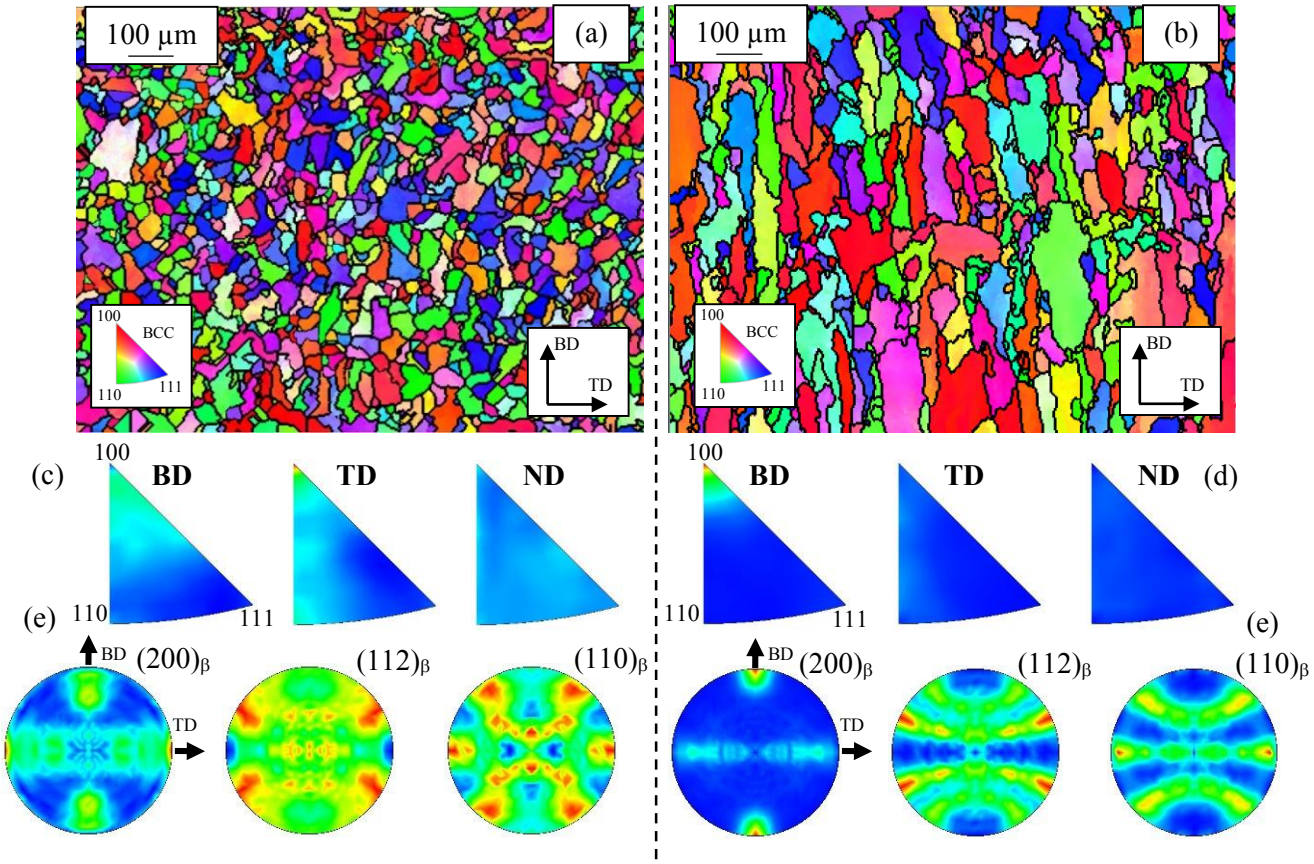

Fig.8: *IPF-EBSD maps along the building direction of the 700WQ state (a) and 400WQ (b) with the pole and inverse pole figures obtained from XRD measurements (c,d,e,f).*

Microstructure of the 400WQ specimen was further characterized by transmission electron microscopy (TEM) to observe the α phase. TEM bright field image (Fig.9) displays a β grain, in which elongated and fine needles are also visible (Fig.9a). These needles are only a dozen nanometres thick, and between 300 nm and 1 µm long. The corresponding SAED (selected area electron diffraction) pattern along the $[011]_\beta$ zone axis (Fig.9b) shows intense spots that correspond to the β phase, with extra lower intensity spots that are indexed as α phase. Due to the standard Burgers orientation relationships (i.e. $(0001)_\alpha$ // $(110)_\beta$, $[2\text{-}1\text{-}10]_\alpha$ // $[1\text{-}11]_\beta$) a single orientation of β phase can lead to six orientations of α phase, usually called variants. The indexation of the diffraction pattern (Fig.9b) exhibits only two α phase variants due to the low-symmetry zone axis considered.

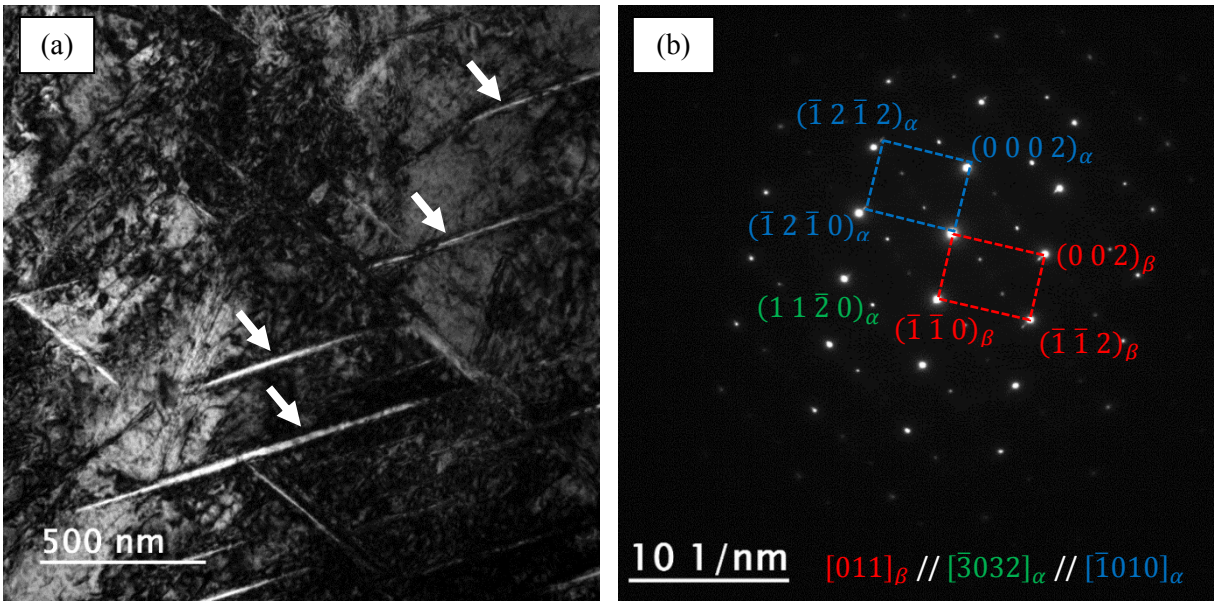

Fig.9: *Bright-field TEM image of the 400WQ specimen microstructure, the α phase laths are highlighted (a), and corresponding indexed diffraction pattern (b).*

3.4. Mechanical characterization by tensile tests

Fig.10 exhibits the engineering stress-strain tensile curves of the different alloys presented in this study. Mechanical characteristics of the different alloys, including Young's modulus, yield and tensile strengths, and maximum elongation are displayed in Table.3.

The AF-Ti-6Al-4V exhibits higher yield and tensile strengths, but lower elongation compared to conventionally wrought Ti-6Al-4V. This can be explained by the fully-α' martensitic microstructure obtained by L-PBF, which is known to display higher strength but lower ductility. However, its Young's modulus is consistent with experimental value of this kind of alloy (~110 GPa). Lack of ductility can limit industrial applications of this titanium alloy in its as-fabricated state. Some leads imply that a decomposition of the martensitic microstructure into a α+β microstructure could happen with carefully selected building

parameters [37]. Otherwise, heat-treatment have shown to be effective to modify the microstructure of additive manufactured Ti-6Al-4V to obtain more interesting properties [41].

The AF-Ti-22Zr-11Nb-2Sn tensile curve exhibits lower mechanical strength than the AF-Ti-6Al-4V ELI, but a much better ductility, reaching a maximum elongation of about 15%. Yield strength, tensile strength and ductility of this alloy correspond to the mechanical behaviour of β-titanium alloys. The AF-Ti-22Zr-11Nb-2Sn tensile curve reveals a Young's modulus of about 50 GPa, which is about twice lower than the Young's modulus of the AF-Ti-6Al-4V ELI. This low Young's modulus is particularly suitable to prevent the stress-shielding effect of biomedical implants such as hip prosthesis or dental implants [10-13, 51].

Despite complete recrystallization, the 700WQ state exhibits mechanical behaviour similar to that of the as-fabricated specimen. However, it should be noted that the Young's modulus is slightly lower in this state, and that the yield strength is also lower than in the as-fabricated state. The decrease of the Young's modulus is consistent with the texture of the 700WQ state, exhibiting a preferential $<100>_{\beta}$ direction along the tensile direction [52, 53]. The lower yield strength comes from the stress-relief during heat-treatment, generating a smoother transition between the elastic and plastic domains.

The mechanical properties of the 400WQ alloy are very different compared to those of AF-Ti-22Zr-11Nb-2Sn and 700WQ Ti-22Zr-11Nb-2Sn alloys (Fig.10). Indeed, the yield and tensile strengths of the 400WQ Ti-22Zr-11Nb-2Sn alloy are comparable to those of the AF-Ti-6Al-4V ELI alloy, and the Young's modulus is slightly higher than the AF-Ti-22Zr-11Nb-2Sn. This enhancement of mechanical properties is due to the precipitation of nano-sized α phase needles in initial β grains which act as a structural hardener inducing higher yield and tensile strengths but reducing ductility. It should be noted that the 400WQ specimen Young's modulus remains low (about 60 GPa) despite the nucleation of α phase.

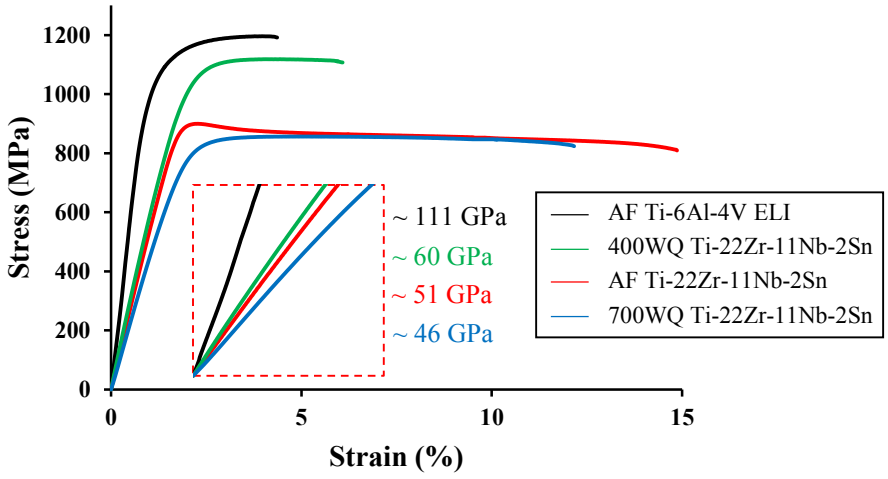

Fig.10: *Engineering stress-strain curves of the AF-Ti-22Zr-11Nb-2Sn (red curve), 400WQ (green curve), 700WQ (blue curve) and AF-Ti-6Al-4V ELI (black curve).*

Table 3
Mechanical characteristics of the different alloys of the present study

	E (GPa)	Re (MPa)	Rm (MPa)	A (%)
AF-Ti-6Al-4V ELI	111±5	972±22	1168±28	3.8±0.5
AF-Ti-22Zr-11Nb-2Sn	51±1	788±19	822±27	14.5±0.4
400WQ	61±7	986±18	1111±30	5.5±0.7
700WQ	46±2	737±24	835±30	12.8±0.8

4. Conclusion

A new β-titanium alloy, the Ti-22Zr-11Nb-2Sn (at%), was successfully elaborated from a blend of elemental powders by *in situ* L-PBF technique. Thanks to the use of DOE, optimized elaboration parameters led to high density samples (>99.3%) with very low fraction of unmelted particles of niobium (<0.05%). Microstructure of the new as-fabricated β-titanium alloy was characterized by XRD and EBSD. Columnar and highly textured <100>$_\beta$ along the building direction microstructure was observed. A low Young's modulus (about 50 GPa) was measured by tensile tests. The microstructure and the mechanical properties of this alloy were compared to those of the Ti-6Al-4V ELI alloy, elaborated by L-PBF technique using pre-alloyed powders. The microstructure of the Ti-6Al-4V ELI alloy being fully martensitic (α' phase), the mechanical characterization displayed low ductility, but high yield and tensile strengths. Texture of the α' martensitic microstructure was also investigated and is consistent with the texture of the high temperature parent β phase from which it formed.

The as-fabricated Ti-22Zr-11Nb-2Sn alloy was heat-treated to modify the microstructure and the mechanical properties. A recrystallization treatment at 700°C was applied successfully, as the microstructure of the 700WQ specimen displayed equiaxed β-grains, with a change in the texture compared to the AF state. However, its mechanical properties remained the same as those of the as-fabricated specimen. A heat-treatment carried out at 400°C has led to a β+α microstructure. TEM observations highlighted the presence of fine α phase needles in β grains. The precipitation of nano-sized α phase needles has led to an improvement of mechanical properties by a precipitation hardening mechanism, reaching a tensile strength comparable to that of the AF-Ti-6Al-4V ELI of the present study, while keeping a low Young's modulus (60 GPa).

This study thus highlights the potential of the *in situ* alloying from elemental powders, and opens a wide range of composition adjustment possibilities. In our case, it shows the capability of the process to produce new highly biocompatible titanium alloys with interesting mechanical properties, combining low Young's modulus and high strength, which are suitable for medical devices.

Acknowledgments:

The authors acknowledge the SCANMAT platforms of the University of Rennes for providing access to XRD, SEM and TEM facilities.

References:

[1] C. Exley, J. Derek Birchall, The cellular toxicity of aluminium, J. Theor. Biol., 159 (1992) 83-98. https://doi.org/10.1016/S0022-5193(05)80769-6

[2] B. C. Costa, C. K. Tokuhara, L. A. Rocha, R. C. Oliveira, P. N. Lisboa-Filho, J. Costa Pessoa, Vanadium ionic species from degradation of Ti-6Al-4V metallic implants: In vitro cytotoxicity and speciation evaluation, Mater. Sci. Eng. C, 96 (2019) 730-739. https://doi.org/10.1016/j.msec.2018.11.090

[3] S.G. Steinemann, Metal implant and surface reactions, Injury, 27 (1996) S/C16-S/C22. https://doi.org/10.1016/0020-1383(96)89027-9

[4] J.P. Luo, Y.J. Huang, J.Y. Xu, J.F. Sun, M.S. Dargusch, C.H. Hou, L. Ren, R.Z. Wang, T. Ebel, M. Yan, Additively manufactured biomedical Ti-Nb-Ta-Zr lattices with tunable Young's modulus: Mechanical property, biocompatibility, and proteomics analysis, Mater. Sci. Eng. C, 114 (2020) 110903. https://doi.org/10.1016/j.msec.2020.110903

[5] V.J. Challis, X. Xu, A. Halfpenny, A.D. Cramer, M. Saunders, A.P. Roberts, T.B. Sercombe, Understanding the effect of microstructural texture on the anisotropic elastic properties of selective laser melted Ti-24Nb-4Zr-8Sn, Acta Mater., 254 (2023) 119021. https://doi.org/10.1016/j.actamat.2023.119021

[6] Y. Okazaki, E. Gotoh, Comparison of metal release from various metallic biomaterials in vitro, Biomaterials, 26 (2005) 11-21. https://doi.org/10.1016/j.biomaterials.2004.02.005

[7] W. Kong, S.C. Cox, Y. Lu, V. Villapun, X. Xiao, W. Ma, M. Liu, M. M. Attallah, The influence of zirconium content on the microstructure, mechanical properties and biocompatibility of in-situ alloying Ti-Nb-Ta based b alloys processed by selective laser melting, Mater. Sci. Eng. C, 131 (2021) 112486. https://doi.org/10.1016/j.msec.2021.112486

[8] R.B. Ashman, S.C. Cowin, W.C. Van Buskirk, J.C. Rice, A continuous wave technique for the measurement of the elastic properties of cortical bone, J. Biomech., 17 (1984) 349-361. https://doi.org/10.1016/0021-9290(84)90029-0

[9] M. Geetha, A.K. Singh, R. Asokamani, A.K. Gogia, Ti based biomaterials, the ultimate choice for orthopaedic implants – A review, Prog. Mater. Sci., 54 (2009) 397-425. https://doi.org/10.1016/j.pmatsci.2008.06.004

[10] B. Van Rietbergen, R. Huiskes, H. Weinans, D.R. Summer, T.M. Turner, J.O. Galante, The mechanism of bone remodeling and resorption around press-fitted THA stems, J. Biomech., 26 (1993) 369-382. https://doi.org/10.1016/0021-9290(93)90001-U

[11] R. Ummethala, P.S. Karamched, S. Rathinavelu, N. Singh, A. Aggarwal, K. Sun, E. Ivanov, L. Kollo, I. Okulov, J. Eckert, K.G. Prashanth, Selective laser melting of high-strength, low modulus Ti-35Nb-7Zr-5Ta alloy, Materialia, 14 (2020) 100941. https://doi.org/10.1016/j.mtla.2020.100941

[12] M. Niinomi, Mechanical properties of biomedical titanium alloys, Mater. Sci. Eng. A, 243 (1998) 231-236. https://doi.org/10.1016/S0921-5093(97)00806-X

[13] M. Niinomi, M. Nakai, J. Hieda, Development of new metallic alloys for biomedical applications, Acta. Biomater., 8 (2012) 3888-3903. https://doi.org/10.1016/j.actbio.2012.06.037

[14] E. Bertrand, T. Gloriant, D.M. Gordin, E. Vasilescu, P. Drob, C. Vasilescu, S.I. Drob, Synthesis and characterisation of a new superelastic Ti-25Ta-25Nb biomedical alloy, J. Mech. Behav. Biomed. Mater., 3 (2010) 559-564. https://doi.org/10.1016/j.jmbbm.2010.06.007

[15] Y.L. Hao, S.J. Li, S.Y. Sun, C.Y. Zheng, R. Yang, Elastic deformation behaviour of Ti-24Nb-4Zr-7.9Sn for biomedical applications, Acta Biomater., 3 (2007) 277-286. https://doi.org/10.1016/j.actbio.2006.11.002

[16] R.L. Batalha, S. Pauly, U. Kühn, K. Kosiba, C. Bolfarini, C.S. Kiminami, P. Gargarella, Oligocrystalline microstructure in an additively manufactured biocompatible Ti-Nb-Zr-Ta alloy, Mater. Lett., 262 (2020) 127149. https://doi.org/10.1016/j.matlet.2019.127149

[17] X. Luo, C. Yang, Z.Q. Fu, L.H. Liu, H.Z. Lu, H.W. Man Z. Wang, D.D. Li, L.C. Zhang, Y.Y. Li, Achieving ultrahigh-strength in beta-type titanium alloy by controlling the melt pool mode in selective laser melting, Mater. Sci. Eng. A, 823 (3.32) 141731. https://doi.org/10.1016/j.msea.2021.141731

[18] J.J. Gao, I. Thibon, P. Castany, T. Gloriant, Effect of grain size on the recovery strain in a new Ti-20Zr-12Nb-2Sn superelastic alloy, Mater. Sci. Eng. A, 793 (2020) 139878. https://doi.org/10.1016/j.msea.2020.139878

[19] P. Castany, T. Gloriant, F. Sun, F. Prima, Design of strain-transformable titanium alloys, C. R. Phys., 19 (2018) 710-720. https://doi.org/10.1016/j.crhy.2018.10.004

[20] D.M. Gordin, F. Sun, D. Laillé, F. Prima, T. Gloriant, How a new strain transformable titanium-based biomedical alloy can be designed for balloon expendable stents, Materialia, 10 (2020) 100638. https://doi.org/10.1016/j.mtla.2020.100638

[21] C-L. Li, J-K. Hong, P.L. Narayana, S-W. Choi, S.W. Lee, C.H. Park, J-T. Yeom, Q. Mei, Realizing superior ductility of selective laser melted Ti-6Al-4V through a multi-step heat treatment, Mater. Sci. Eng. A, 799 (2021) 140367. https://doi.org/10.1016/j.msea.2020.140367

[22] D. Zhang, L. Wang, H. Zhang, A. Maldar, G. Zhu, W. Chen, J-S. Park, J. Wang, X. Zeng, Effect of heat treatment on the tensile behavior of selective laser melted Ti-6Al-4V by in situ X-ray characterization, Acta Mater., 189 (2020) 93-104. https://doi.org/10.1016/j.actamat.2020.03.003

[23] N. Jin, Z. Yan, Y. Wang, H. Cheng, H. Zhang, Effects of heat treatment on microstructure and mechanical properties of selective laser melted Ti-6Al-4V lattice materials, Int. J. Mech. Sci., 190 (2021) 106042. https://doi.org/10.1016/j.ijmecsci.2020.106042

[24] B. Vrancken, L. Thijs, J.-P. Kruth, J. Van Humbeeck, Microstructure and mechanical properties of a novel β titanium metallic composite by selective laser melting, Acta Mater., 68 (2014) 150-158. https://doi.org/10.1016/j.actamat.2014.01.018

[25] M. Fischer, D. Joguet, G. Robin, L. Peltier, P. Laheurte, In situ elaboration of a binary Ti-26Nb alloy by selective laser melting of elemental titanium and niobium mixed powders, Mater. Sci. Eng. C, 62 (2016) 852-859. https://doi.org/10.1016/j.msec.2016.02.033

[26] D. Gu, W. Meiners, Microstructure characteristics and formation mechanisms of in situ WC cemented carbide based hardmetals prepared by selective laser melting, Mater. Sci. Eng. A, 527 (2010) 7585-7592. https://doi.org/10.1016/j.msea.2010.08.075

[27] W. Chen, C. Chen, X. Zi, X. Cheng, X. Zhang, Y.C. Lin, K. Zhou, Controlling the microstructure and mechanical properties of a metastable β titanium alloy by selective laser melting, Mater. Sci. Eng. A, 726 (2018) 240-250. https://doi.org/10.1016/j.msea.2018.04.087

[28] D. Zhao, C. Han, J. Li, J. Liu, Q. Wei, *In situ* fabrication of a titanium-niobium alloy with tailored microstructures, enhanced mechanical properties and biocompatibility by using selective laser melting, Mater. Sci. Eng. C, 111 (2020) 110784. https://doi.org/10.1016/j.msec.2020.110784

[29] S.L. Sing, W.Y. Yeong, F.E. Wiria, Selective laser melting of titanium alloy with 50 wt% tantalum: Microstructure and mechanical properties, J. Alloys Compd., 660 (2016) 461-470. https://doi.org/10.1016/j.jallcom.2015.11.141

[30] E.G. Brodie, A.E. Medvedev, J.E. Frith, M.S. Dargusch, H.L. Fraser, A. Molotnikov, Remelt processing and microstructure of selective laser melted Ti25Ta, J. Alloys Compd., 820 (2020) 153082. https://doi.org/10.1016/j.jallcom.2019.153082

[31] S. Huang, R. Lakshmi Narayan, J. Heang Kuan Tan, S.L. Sing, W.Y. Yeong, Resolving the porosity-unmelted inclusion dilemma during in-situ alloying of Ti34Nb via laser powder bed fusion, Acta Mater., 204 (2021) 116522. https://doi.org/10.1016/j.actamat.2020.116522

[32] J.C. Wang, Y.J. Liu, P. Qin, S.X. Liang, T.B. Sercombe, L.C. Zhang, Selective laser melting of Ti-35Nb composite from elemental powder mixture: Microstructure, mechanical behavior and corrosion behavior, Mater. Sci. Eng. A, 760 (2019) 214-224. https://doi.org/10.1016/j.msea.2019.06.001

[33] K. Endoh, M. Tahara, T. Inamura, H. Hosoda, Effect of Sn and Zr content on superelastic properties of Ti-Mo-Sn-Zr biomedical alloys, Mater. Sci. Eng. A, 704 (2017) 72-76. https://doi.org/10.1016/j.msea.2017.07.097

[34] Y.L. Hao, S.J. Li, S.Y. Sun, R. Yang, Effect of Zr and Sn on Young's modulus and superelasticity of Ti-Nb based alloys, Mater. Sci. Eng. A, 441 (2006) 112-118. https://doi.org/10.1016/j.msea.2006.09.051

[35] L. Thijs, F. Verhaeghe, T. Craeghs, J. Van Humbeeck, J.-P. Kruth, A study of the microstructural evolution during selective laser melting of Ti-6Al-4V, Acta Mater., 58 (2010) 3303-3312. https://doi.org/10.1016/j.actamat.2010.02.004

[36] H. Gong, K. Rafi, H. Gu, T. Starr, B. Stucker, Analysis of defect generation in Ti-6Al-4V parts made using powder bed fusion additive manufacturing processes, Addit. Manuf., 1-4 (2014) 87-98. https://doi.org/10.1016/j.addma.2014.08.002

[37] A. Zafari, M.R. Barati, K. Xia, Controlling martensitic decomposition during selective laser melting to achieve best ductility in high strength Ti-6Al-4V, Mater. Sci. Eng. A, 744 (2019) 445-455. https://doi.org/10.1016/j.msea.2018.12.047

[38] G. Kasperovich, J. Haubrich, J. Gussone, G. Requena, Correlation between porosity and processing parameters in TiAl6V4 produced by selective laser melting, Mater. Des., 105 (2016) 160-170. https://doi.org/10.1016/j.matdes.2016.05.070

[39] P. Liu, Z. Wang, Y. Xiao, M.F. Horstemeyer, X. Cui, L. Chen, Insight into the mechanisms of columnar to equiaxed grain transition during metallic additive manufacturing, Addit. Manuf., 26 (2019) 22-29. https://doi.org/10.1016/j.addma.2018.12.019

[40] A. Khorasani, I. Gibson, U.S. Awan, A. Ghaderi, The effect of SLM process parameters on density, hardness, tensile strength and surface quality of Ti-6Al-4V, Addit. Manuf., 25 (2019) 176-186. https://doi.org/10.1016/j.addma.2018.09.002

[41] B. Vrancken, L. Thijs, J.-P. Kruth, J. Van Humbeeck, Heat treatment of Ti6Al4V produced by selective laser melting: Microstructure and mechanical properties, J. Alloys Compd., 541 (2012) 177-185. https://doi.org/10.1016/j.jallcom.2012.07.022

[42] J. Metelkova, Y. Kinds, K. Kempen, C. de Formanoir, A. Witvrouw, B. Van Hooreweder, On the influence of laser defocusing in selective laser melting of 316L, Addit. Manuf., 23 (2018) 161-169. https://doi.org/10.1016/j.addma.2018.08.006

[43] D. Herzog, V. Seyda, E. Wycisk, C. Emmelmann, Additive manufacturing of metals, Acta Mater., 117 (2016) 371-392. https://doi.org/10.1016/j.actamat.2016.07.019

[44] E. Vasquez, P.-F. Giroux, F. Lomello, A. Chniouel, H. Maskrot, F. Schuster, P. Castany, Elaboration of oxide dispersion strengthened Fe-14Cr stainless steel by selective laser melting, J. Mater. Process Technol., 267 (2019) 403-413. https://doi.org/10.1016/j.jmatprotec.2018.12.034

[45] L. Zhou, T. Yuan, R. Li, J. Tang, M. Wang, F. Mei, Anisotropic mechanical behavior of biomedical Ti-13Nb-13Zr alloy manufactured by selective laser melting, J. Alloys Compd, 762 (2018) 289‑300. https://doi.org/10.1016/j.jallcom.2018.05.179

[46] M. Simonelli, Y.Y. Tse, C. Tuck, On the Texture Formation of Selective Laser Melted Ti-6Al-4V, Metall. Mater. Trans. A., 45 (2014) 2863-2872. https://doi.org/10.1007/s11661-014-2218-0

[47] T. Gloriant, G. Texier, F. Sun, I. Thibon, F. Prima, J.L. Soubeyroux, Characterization of nanophase precipitation in a metastable β titanium-based alloy by electrical resistivity, dilatometry and neutron diffraction, Scr. Mater., 58 (2008) 271-274. https://doi.org/10.1016/j.scriptamat.2007.10.007

[48] R. Dong, J. Li, J. Fan, H. Kou, B. Tang, Precipitation of α phase and its morphological evolution during continuous heating in a near β titanium alloy Ti-7333, Mater. Charact., 132 (2017) 199-204. https://doi.org/10.1016/j.matchar.2017.07.032

[49] N. Kalentics, E. Boillat, P. Peyre, C. Gorny, C. Kenel, C. Leinenbach, J. Jhabvala, R.E. Logé, 3D laser shock peening – a new method for the 3D control of residual stresses in selective laser melting, Mater. Des., 130 (2017) 350-356. https://doi.org/10.1016/j.matdes.2017.05.083

[50] B. Ahmad, S. O. van der Veen, M. E. Fitzpatrick, H. Gao, Residual stress evaluation in selective-laser-melting additively manufactured titanium (Ti-6Al-4V) and inconel 718 using the contour method and numerical simulation, Addit. Manuf., 22 (2018) 571-582. https://doi.org/10.1016/j.addma.2018.06.002

[51] T. Nishino, H. Mishima, H. Kawamura, Y. Shimizu, S. Miyakawa, N. Ochiai, Follow-up results of 10-12 years after total hip arthroplasty using cementless tapered stem – frequency of severe stress shielding with synergy stem in Japanese patients, J. Arthroplasty, 28 (2013) 1736-1740. https://doi.org/10.1016/j.arth.2013.02.027

[52] H. Jabir, A. Fillon, P. Castany, T. Gloriant, Crystallographic orientation dependence of mechanical properties in the superelastic Ti-24Nb-4Zr-8Sn alloy, Phys. Rev. Mater., 3 (2019) 063608. https://doi.org/10.1103/PhysRevMaterials.3.063608

[53] S.-H. Lee, M. Todai, M. Tane, K. Hagihara, H. Nakajima, T. Nakano, Biocompatible low Young's modulus achieved by strong crystallographic elastic anisotropy in Ti-15Mo-5Zr-3Al alloy single crystal, J. Mech. Behav. Biomed. Mater., 14 (2012) 48-54. https://doi.org/10.1016/j.jmbbm.2012.05.005